metals

MDPI

Article

Investigating Nanoscale Contact Using AFM-Based Indentation and Molecular Dynamics Simulations

Shyamal Roy [1,2,†], Sönke Wille [3,†], Dan Mordehai [1] and Cynthia A. Volkert [3,*]

[1] Department of Mechanical Engineering, Technion—Israel Institute of Technology, Haifa 3200003, Israel; s.roy@fz-juelich.de (S.R.); danmord@me.technion.ac.il (D.M.)
[2] Institute for Advanced Simulation, Materials Data Science and Informatics (IAS-9), Forschungszentrum Jülich GmbH, 52425 Jülich, Germany
[3] Institute of Materials Physics, University of Göttingen, 37077 Göttingen, Germany; soenke.wille@web.de
* Correspondence: cynthia.volkert@phys.uni-goettingen.de
† These authors contributed equally to this work.

Abstract: In this work we study nanocontact plasticity in Au thin films using an atomic force microscope based indentation method with the goal of relating the changes in surface morphology to the dislocations created by deformation. This provides a rigorous test of our understanding of deformation and dislocation mechanisms in small volumes. A series of indentation experiments with increasing maximum load was performed. Distinct elastic and plastic regimes were identified in the force-displacement curves, and the corresponding residual imprints were measured. Transmission electron microscope based measured dislocation densities appear to be smaller than the densities expected from the measured residual indents. With the help of molecular dynamics simulations we show that dislocation nucleation and glide alone fail to explain the low dislocation density. Increasing the temperature of the simulations accelerates the rate of thermally activated processes and promotes motion and annihilation of dislocations under the indent while transferring material to the upper surface; dislocation density decreases in the plastic zone and material piles up around the indent. Finally, we discuss why a significant number of cross-slip events is expected beneath the indent under experimental conditions and the implications of this for work hardening during wear.

Keywords: thermally activated processes; contact mechanics; nanoindentation; atomic force microscopy; molecular dynamics simulations

Citation: Roy, S.; Wille, S.; Mordehai, D.; Volkert, C.A. Investigating Nanoscale Contact Using AFM-Based Indentation and Molecular Dynamics Simulations. *Metals* **2022**, *12*, 489. https://doi.org/10.3390/met12030489

Academic Editor: Alain Pasturel

Received: 31 January 2022
Accepted: 28 February 2022
Published: 14 March 2022

1. Introduction

Nanoindentation is an important tool to observe the mechanical properties and the deformation behavior of materials. Due to the possibility to exert small local forces, indentation with atomic force microscopes (AFM) is widely used to study deformation in soft matter (e.g., [1–3]) and thin and composite hard materials (e.g., [4–6]). Furthermore, AFM imaging of the deformed surfaces can provide insights into the deformation mechanisms [7–13]. The onset of plasticity in metals is normally identified by deviations from Hertzian contact by the occurrence of "pop-ins" in the force-depth curves [14,15]. Using AFM indentation on gold bulk, pop-ins were observed by Asenjo et al., which they explained by the generation and movement of dislocation loops [7]. Lilleodden and Nix showed that the initial dislocation density in Au thin films needs to be low for these pop-ins to occur [16]. Transmission electron microscopy (TEM) investigations of indents in Ni and Al show a high density of dislocations directly under the indent and the emission of prismatic loops and helix dislocations [17,18].

For shallow indents, the Nix-Gao model relates the indentation forces through the hardness to the plastic zone generated beneath the indent [19]. The model suggests that dislocation prismatic loops are nucleated under the indenter tip and move downwards into the bulk to match the geometry of the indent. Both statistically stored and geometrically

necessary dislocations contribute to the hardness. While this model successfully captures the indentation size effect at shallow indents, computer simulations demonstrate that the deformation mechanisms are more complex. In particular, the onset of plasticity was found to be related to homogeneous nucleation of glissile dislocation loops beneath the indent (e.g., [20–22]). The loops grow and react with other glissile dislocation loops. As a result, a complex sessile dislocation microstructure is formed beneath the indents. In the case of face-centered cubic metals, with the occurrence of cross-slip events, reactions form dislocation prismatic loops that glide in all <111> directions [23–25]. When indenting a (111) surface, full loops glide along <111> directions that are not parallel to the indented surface. However, half prismatic loops are formed at later stages. These half loops terminate at both ends on the indented surface and glide parallel to it [25]. Under the applied load, these loops glide away from the indent, and unless they react with other defects or free surfaces, removing the load will allow some of the full prismatic loops to be attracted to the surface and glide back to the indent.

Despite the naïve approach of the Nix-Gao model as to the type and direction of the nucleated dislocations, it allows the calculation of the average dislocation density in the plastic zone. Based on this model, the dislocation density is inversely proportional to the indentation depth. At indentation depths of a few hundred nanometers and more, the values obtained for the dislocation density from the model are slightly higher than observed in experiments (by less than an order of magnitude). Different reasons for this have been proposed in literature. For instance, Durst et al. showed using finite element analysis that the plastic zone extends deeper than assumed in the model [26]. They revisited the model accordingly, resulting in a slightly lower dislocation density. A study of the dislocation structure around indents in Twinning Induced Plasticity (TWIP) metals, showed that the plastic zone extends laterally, as opposed to the assumption that it terminates outside the contact region with the tip [27]. However, at shallow indents of a few tens of nanometers, the model predicts extremely high dislocation densities. Even at plastic zones of a few tens of nanometers, which are expected near shallow indents, the predicted values of the dislocation density are high and the corresponding distance between dislocations is of only several nanometers. Thus, if dislocation nucleation and glide are the predominant mechanisms, one would expect to see large dislocation densities even around shallow indents.

In this work we aim to understand plasticity during very shallow indents between an AFM tip and a Au thin film. In Section 2 we discuss the experimental and computational methods employed in this work. Then we detail in Section 3.1 the observations of the AFM-based nanoindentation experiments. The plasticity induced during contact was evaluated both with AFM and TEM imaging, revealing a discrepancy between residual indent volumes and dislocation densities. We then address this question with high-temperature molecular dynamics (MD) simulations in Section 3.2 to show that this may be a result of thermally activated processes in the dislocation structure beneath the contact. Finally, in Section 4 we bridge between the MD and the experimental time- and temperature-scales to estimate the importance of cross-slip in the experimental conditions.

2. Materials and Methods

2.1. Experimental

Polycrystalline gold thin films of nominal thicknesses of 50 nm, 100 nm, and 200 nm deposited by magnetron sputtering on polished and planar mica substrates (Phasis) were purchased for the studies. Au was selected due to the fact that it does not oxidize so that the dislocation slip traces are easily visible with AFM. Electron Backscatter Diffraction measurements performed with a Channel 5 (Oxford Instruments, Abingdon, UK) revealed only grains with [111] out of plane orientations and with random in plane orientations. The grain sizes in the 200 nm film ranged from 500 nm to 5 µm, in the 100 nm thick film from 300 nm to 3 µm and in the 50 nm thick film from 100 nm to 2 µm. While the 200 nm and 100 nm films are continuous, the 50 nm films are discontinuous and contain regions of

bare substrate making up approx. 5% of the total area. TEM studies on a CM30 (Philips, Eindhoven, The Netherlands) of focused ion beam (FIB) prepared cross-sections show that the true thicknesses are 200, 100, and 60 nm and that the films are almost dislocation free and rarely contain twins. An Asylum MFP-3D AFM (Oxford Instruments, Abingdon, UK) operating at ambient conditions was used for imaging and indenting the samples. Si cantilevers with a coating of diamond like carbon (DLC190, Budget Sensors, Sofia, Bulgaria) were used, due to their improved hardness relative to uncoated tips. The tip radius was about 50 nm, as measured with scanning electron microscopy. The absolute deflection of the cantilever tips was calibrated from force-distance curves on sapphire. The spring constant of the cantilever was determined from the thermal resonance frequency [28]. The influence of a lateral motion of the tip during the indentation was investigated by a series of additional measurements performed in a Veeco AFM (Veeco, Plainview, NY, USA), where lateral motion of the tip was compensated.

2.2. Computational

A nanoindentation model setup is created as shown schematically in Figure 1. A thin film is indented by a spherical virtual indenter of radius 3.6 nm on its (111) surface (Figure 1). The indenter is defined by a repulsive force field that is zero beyond its geometry. The bottom surface of atoms is fixed in the $[111]$ crystallographic orientation (z axis) and the film is periodic in $[\bar{1}\bar{1}2]$ (x) and $[1\bar{1}0]$ (y) crystallographic directions. The system period is in the x and y directions and is 30 nm in each direction. The thin film height is 14.6 nm. The top surface is a free surface. The embedded-atom method (EAM) interatomic potential, with the parametrization proposed by Grochola et al. for Au, is employed [29]. The simulation is performed in several steps:

- Static relaxation at 10 K by the conjugate gradient.
- Relaxation at 10 K via 30,000 MD time steps with a time step of 3 fs.
- Indentation of the film at 10 K at a constant rate of 0.01 $\frac{\text{nm}}{\text{ps}}$, up to a depth equal to 3.36 nm. Once reaching the maximum depth, the indenter is kept static during the following steps.
- Heating the system up to the target temperature between 200 K and 1100 K, which is lower than the melting point, using the Nosé-Hoover thermostat during 100,000 MD time steps. In combination with the Parrinello-Rahman dynamics, the volume is allowed to change. We note that the global pressures P_{xx} and P_{yy} are not set to zero but fixed at the values reached at the end of indentation (previous step). This accelerates all thermally activated processes while ensuring that the effect of thermal expansion on the relaxation of the internal stresses generated during indentation is minimized.
- The simulation is continued in the constant-temperature constant-stress ensemble for 400,000 additional MD time steps, in order to allow thermally activated processes to take place.
- During the last two stages, replicas of the system are quenched periodically via conjugate gradient. The quenched systems are employed to identify and visualize the dislocation structures via the common neighbor analysis.

We note that the protocol of indenting at 10 K and subsequently heating to a final high temperature allows us to distinguish between processes resulting from purely mechanical interactions and those that are facilitated by thermal activation. The first indentation stage is performed at low temperature to generate the initial dislocation microstructure with minimum effect of thermally activated processes. Then, heating the sample to different temperatures, without removing the indent, allows us to compare the effect of thermally activated processes on the dislocation structure, starting from the same initial dislocation structure. The high temperature in the simulation, as opposed to room temperature in which the experiments is performed, allows an approximate treatment of thermal relaxation at the experimental time scale of seconds, which is otherwise not accessible given the current nanosecond time scale for MD simulations.

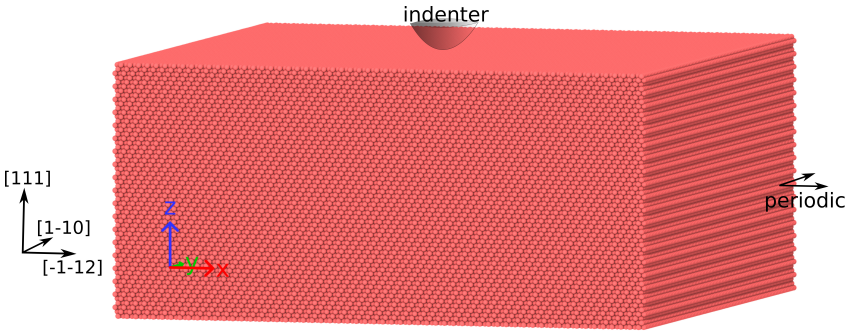

Figure 1. A schematic illustration of the atomistic model. The indentation is performed into the $[\bar{1}\bar{1}\bar{1}]$ crystallographic orientation with periodic boundaries in the $[\bar{1}\bar{1}2]$ and $[1\bar{1}0]$ directions.

3. Results

3.1. Experimental Results

3.1.1. Indentation Curves

In a typical experiment, a suitable area of the sample with relatively large grains was selected and the topography characterized by imaging in intermittent contact tapping mode. The grain boundaries could be identified by grooves. Then a series of indentations with increasing maximum force (from 1 µN to 10 µN in 1 µN steps) was performed at selected sites, normally within one grain. The indentation depth was calculated from the difference between the cantilever deflection and z-piezo extension. The lateral movement of the tip due to the deflection of the cantilever was not compensated. After indentation, the surface topography was scanned again. To highlight the changes in topography due to the indents, drift corrected difference images were calculated. All measurements were performed with a single cantilever. The force-depth curves for several indents with maximum forces between 1 µN and 5 µN are shown in Figure 2. Distinct regions can be identified in the curves, consistent with previous studies in the literature [12,30]. Region I is primarily attributed to elastic loading where the slope is determined by the increasing contact area and the stiffnesses of the film and tip. Region II is primarily attributed to plastic deformation of the film where the slope is controlled by a combination of the increasing contact area and work hardening (or softening) of the film material. The small strain bursts evident in this region (several are indicated with arrows) are typically attributed to larger plastic events [14]. Region III shows elastic unloading with a slope that is somewhat smaller than in Region I, at least for the deeper indents. It is believed that the contact area of a plastically deformed volume remains fairly constant on initial unloading and only the stiffnesses contribute to the slope.

Region IV is only occasionally reported in the literature [31] and its origins have not yet been discussed. We were able to significantly reduce the magnitude of region IV by compensating for the lateral tip movement during indentations performed in an Veeco AFM. Thus, we propose that region IV is caused by the lateral motion of the tip on unloading and the resultant sliding friction between the tip and the sidewalls of the indent. Further, we observe that region IV is present for all materials we have investigated thus far (including bulk Au, and Al and Pt thin films), supporting the idea of an effect of the testing geometry instead of a material property.

All five curves show a high reproducibility in that the slopes in the elastic and the plastic regimes are the same and indentations with the same maximum force lead to very similar indentation depths. This implies that the tip shape remains unchanged during the indentation series and allows quantitative comparisons between tests.

Figure 2b shows force depth curves obtained from indentations of the 50, 100, and 200 nm thick films to a maximum force of 10 µN, all performed with the same tip. In this experiment the 200 nm film was indented first, then the 100 nm and the 50 nm thick films. In the end, the 200 nm film was indented again to check for reproducibility. Since the two curves for the 200 nm films are almost identical, we attribute the differences between the

curves in Figure 2b to the film thickness. All three film thicknesses show the same elastic loading slope and the same force and depth for the onset of plasticity. In addition, the unloading slopes in region III and region IV are almost identical. Even the plastic response (region II) up to a depth of 30 nm is the same for all film thicknesses. Only when the indent depth reaches a value of around two-thirds of the film thickness, do we observe a difference in the plastic response. The larger forces needed at a given depth in the thinner films relative to the thicker films seems likely due to the influence of the substrate which is harder and less compliant than the Au films. TEM images of a FIB cross-section of the indent into the 50 nm film confirm that the imprint reaches down to the substrate.

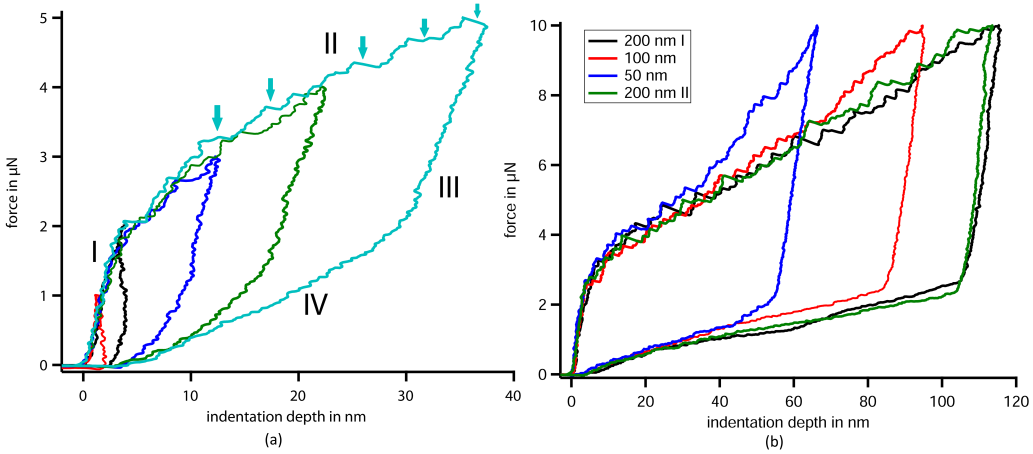

Figure 2. (**a**) Force-displacement curves for five atomic force microscope (AFM) indentations to different maximum forces into a 200 nm gold thin film. The onset of plasticity at 2 µN is consistent with the occurrence of a residual imprint. (**b**) Force-displacement curves to a maximum force of 10 µN performed with a single AFM tip into films of different thicknesses. Indents were performed first and last in the 200 nm thick films, to confirm reproducibility. The curves all initially show the same behavior, until the tip almost reaches the substrate, indicating that the initial plastic response is independent of the film thickness.

3.1.2. Post-Indentation Surface Topography

Figure 3 shows the sample area topography before and after the five indents in Figure 2a, as well as the drift corrected difference between the images. The indentation with the 1 µN maximum force did not leave any detectable change in topography, which is consistent with the absence of plasticity (region II) in the force depth curve. The 2 µN indentation caused a 2 nm deep imprint with no evidence of material piled up around the imprint. The indentations with higher maximum forces produced larger and deeper imprints with some pile-up. By comparing imprints from different grains (not shown here) we note that the shapes of the imprints and pile-ups are fairly consistent within one grain but vary from grain to grain, suggesting that they are dependent on the relative orientations between the tip and the grain crystallographic directions.

An investigation of the imprint and pile-up shapes for the different film thicknesses also shows no clear effect of film thickness (not shown here). Indentation on a bulk Au sample showed the same behavior as the 200 nm film, when indented with the same tip. So apart from the direct contribution of hardness of the substrate, no thickness effect in the deformation behavior was observed.

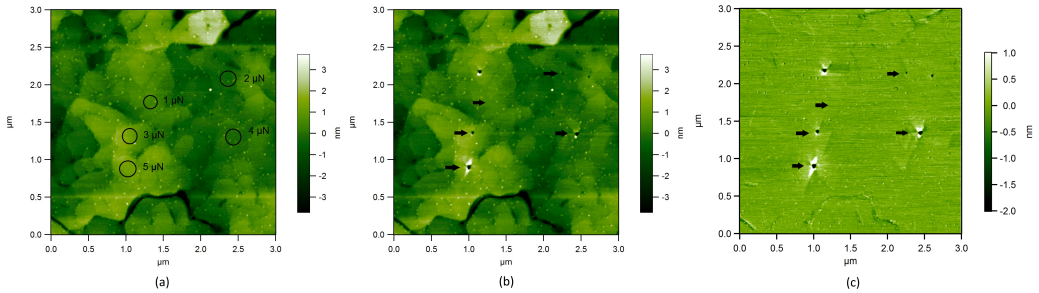

Figure 3. AFM image of a 200 nm thin film before (**a**) and after (**b**) a series of indentations; (**c**) shows the difference of (**a**,**b**). For forces above 1 µN, one can clearly see pile-up of material around the residual imprint.

In some experiments on the 200 nm films long range surface traces originating from the indents were found (Figure 4a). The traces are perfectly straight and have a height of approx. 230 pm which is consistent with the distance between (111) planes in gold of 233 pm. The traces have angles of 60° to each other, which corresponds to the angle of a (111) planes intersecting the [111] surface plane indicating the theses traces are connected to the crystallography of the sample. In experiments that showed traces, on average two lines were created per indent. No such traces were found in the 100 nm and 50 nm films.

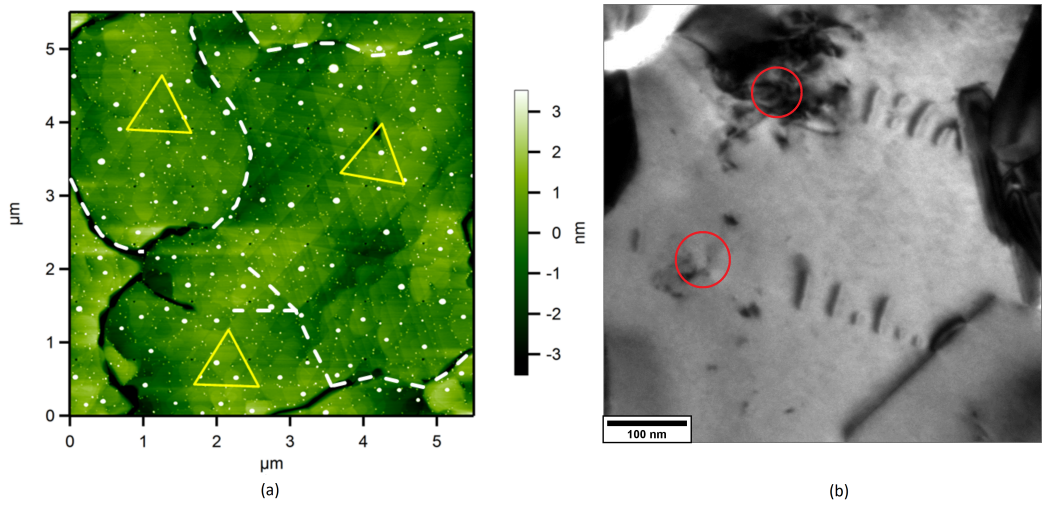

Figure 4. (**a**) Array of 7 × 7 indentations with a maximum force of 5 µN in an 200 nm gold thin film. These indentations create long range surface steps with a height corresponding to the (111) plane in gold. The yellow triangles show the orientations of the glide traces in the different grains whose boundaries are indicated by dashed white lines. (**b**) Dislocation structures surrounding two indentations in a 150 nm gold film on SiN_x.

3.1.3. Post-Indentation Dislocation Structure

To investigate the dislocation structures in the samples after indentations, a Au film with a thickness of approx. 150 nm was grown on SiN_x membranes by pulsed laser deposition to provide a plan view sample without additional preparation. Despite the different deposition technique these films showed a similar deformation behavior with comparable indent morphology and force-depth curves (performed on the support frame next to the membrane). After selecting defect-free grains with (111) out of plane orientations in the TEM, several grains were indented and re-investigated in the TEM. A TEM bright field image of a grain containing two indents is shown in Figure 4b. No dislocations are visible directly under the smaller indent. The larger indent shows a few dislocations. From additional TEM weak beam dark field images, the number was estimated as 10–15. This number, consistent with TEM cross sectional images of an indented gold film on mica,

is surprisingly low. A simple model gives a minimum required number of dislocations that scales linearly with indent depth, which is at least an order of magnitude larger than our observations. For instance, 180 dislocations are expected to nucleate in order to indent the tip to a depth of 12 nm (corresponds to a maximum force of 3 μN). For a maximum force of 7 μN and an indentation depth of 70 nm, 1080 dislocations are expected. Additionally, the TEM image shows several dislocations are arranged along a straight line and apparently piled up against a grain boundary. In order to understand the discrepancy between the counted dislocation number and the imprint volume, we performed molecular dynamics simulations.

3.2. Computational Results

3.2.1. Forming the Plastic Zone Beneath the Indenter

MD simulations are customarily utilized to study nanoindentation due to their ability to naturally describe dislocation nucleation and glide during plastic deformation. After relaxing the system, the indentation is performed at a constant rate and at a low temperature of 10 K, while dislocation formation and evolution are tracked and analyzed. Such a simulation allows exploring whether dislocation nucleation and glide are sufficient to understand the relatively dilute dislocation structure beneath the indent. We chose here the film thickness of 14.6 nm. Based on the work of Kositski and Mordehai [22] this ratio between film thickness and indenter radius is sufficient to eliminate the influence of film thickness. To demonstrate this, the loading and unloading simulations for different film thicknesses are shown in Figure 5. There are some small effects of film thickness in the elastic regime for the 6.8 nm thick film. However, the general trend in the plastic regime is the same. At the early stages of the plastic deformation, most of the dislocations are nucleated on slip planes which are parallel to the upper surface. As an example, we show in Figure 6 the dislocation structure at an indentation depth of 1.5 nm.

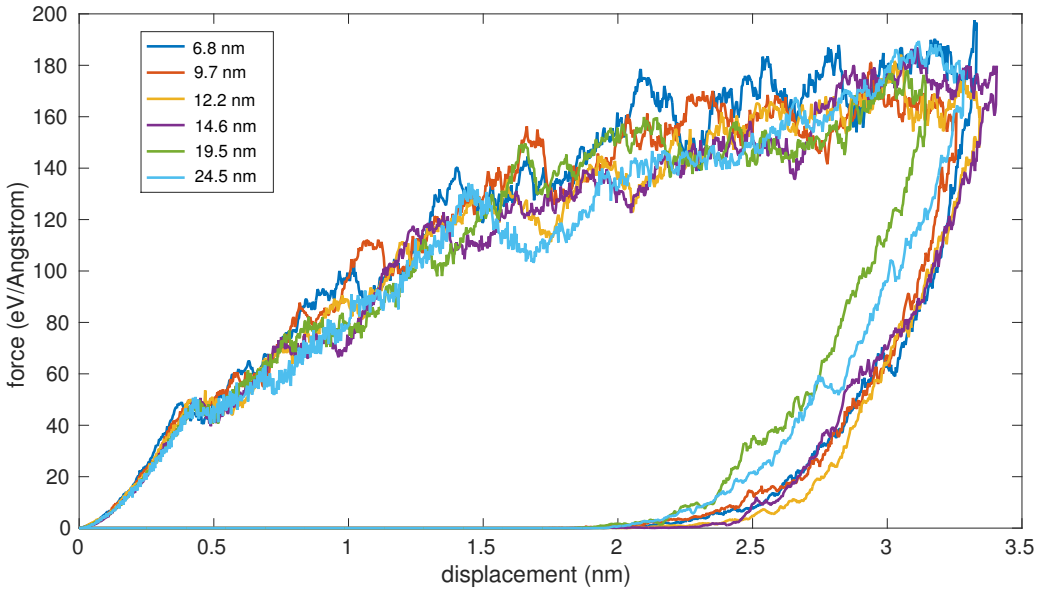

Figure 5. Force-displacement curves during loading and unloading of different film thicknesses. The deviation in the unloading curves is due to the different indentation depths for different film thicknesses.

Most of the dislocations are dissociated, with some constricted segments along highly jogged regions. The Burgers vectors of all dislocations are parallel to the upper surface, which we denote as in-plane. Some of the in-plane dislocations interact and remain around the indent. But if both ends terminate on the top surface, the in-plane dislocations form half prismatic loops which glide easily laterally from the indent in an in-plane direction. In the simulations, these half prismatic loops do not leave the computational cell due to the

periodic boundary conditions. In practice, these loops are expected to glide away from the indent and may be absorbed in grain boundaries [32] or free surfaces [33]. There are also some stacking fault "islands" formed parallel to and just below the upper surface. These islands can also glide in the (111) plane and can be regarded as in-plane dislocations of a height of one atomic layer. In summary, up to this stage, in-plane dissociated dislocations are nucleated and formed, and they glide laterally away from the plastic zone. As the tip is further indented, at an indentation depth of 2.4 nm, dislocations are nucleated and glide in directions that are not parallel to the upper surface, which we denote as out-of-plane. An example for a dislocation in an out-of-plane direction, is shown in Figure 6b. Dissociated dislocations with Burgers vectors 1/2[101] are nucleated beneath the indent on $(\bar{1}1\bar{1})$ and $(11\bar{1})$ planes. The collinear interaction between these dislocation segments causes them to glide easily downwards, away from the free surface. This shape was observed in many MD simulations of the nanoindentation of FCC metals and is proposed to lead eventually to prismatic loop formation, which than glide in out-of-plane directions [25]. As an example, the dislocations marked by 'A' and 'B' in Figure 6c at 3.36 nm indentation depth, are appearing to close a prismatic loop.

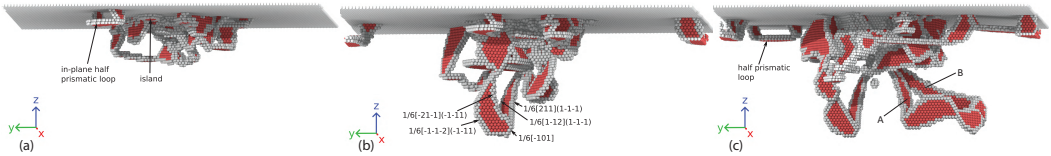

Figure 6. Indentation of a thin film at 10 K. The dislocation structure during indentation is shown at indentation depths of (**a**) 1.5 nm, (**b**) 2.4 nm and (**c**) 3.36 nm. See text for more details on the evolution of dislocations in the in-plane and out-of-plane directions.

At the end of the indentation (at the indentation depth 3.36 nm), a complex and dense dislocation structure is created beneath the indent as shown in Figure 6c. The in-plane dislocations remain at the upper part of the thin film and are of a typical dimension that corresponds to the indentation depth. The number of dislocations in out-of-plane directions is increasing. The out-of-plane dislocations interact and form on intersecting (111) planes, forming jogs along the dislocation lines, constricted dislocation segments. Removal of the periodic boundary conditions or a thicker film may allow the half/full prismatic loops to form and glide away from the indent in the in-plane or out-of-plane directions, respectively. However, this does not undermine the fact that many dislocations remain bundled around the indent, in both in- and out-of-plane directions, forming the plastic zone. An indication of the dislocation activity is the material pile-up on the free surface. Most of the volume pushed by the indent is transferred into the bulk in the form of dislocations. In other words, the in-plane and out-of-plane directions transfer material via dislocation glide laterally and downwards, respectively. Thus, dislocation nucleation and glide alone is insufficient to explain the low dislocation densities in the experiment, and dislocation annihilation inside the film could be the predominant mechanism that decrease the dislocation densities.

The dislocation structures obtained in MD simulations at 10 K and nanosecond time scales cannot be directly compared with the room temperature indents performed on the time scale of seconds. At these times and at the stresses that develop inside the specimen, thermally activated processes may prevail. In particular, cross-slip of the screw segments may lead to dislocation annihilation. Cross-slip, which is a process in which screw dislocations change slip planes, requires overcoming an energy barrier and normally in the time frames of MD simulations, cross-slip events are rare. Consequently, in order to stimulate cross-slip events, the indented film was heated to high temperatures, without removing the load. While the temperatures in the simulations are beyond the temperature in the experiments, it allows sufficient cross-slip events during the simulation time frame, in order to examine how it alters the dislocation microstructure in the plastic zone. We emphasize that the high temperatures aim at promoting cross-slip in the MD simulations,

rather than providing any quantitative estimation on the rate by which these events occur in the experiments.

3.2.2. Microstructure Evolution in Heated Thin films

The indented system is heated up, while keeping the indenter in place, and then the temperature was maintained constant for 1.2 ns. During this time, the stress acting on the lateral dimensions of the computational cell was kept constant (which is not zero, due to the indentation), in order to allow for the thermal expansion while not removing the stress imposed by the indenter. The system was heated to various temperatures between 200 K and 1100 K. The total dislocation length was calculated during the simulation by summing the total perfect dislocation lengths and half of the total partial dislocation lengths. While the absolute value of the total dislocation length in the simulation is meaningless, dividing the length by the total length prior to the heating allows us to quantify the change of dislocation densities during heating. One can see that for all temperatures the dislocation density decreases with time as shown in Figure 7. We note the dislocation annihilation commences as we increase the temperature, even before bringing the temperature of the system to equilibrium. Nonetheless, the effect of temperature is pronounced; at 200 K the dislocation density only decreases slightly whereas the dislocation annihilation rate is higher at higher temperatures. The dislocation microstructure during heating to 900 K is shown chronologically in Figure 8. As the temperature is increased, the plastic zone beneath the indent decreases. When temperature reaches 900 K most of the out-of-plane dislocations are annihilated and reach steady state, as shown in Figure 8d. From the initial complex dislocation structure beneath the indent, there are only a few dislocations left, with some vacancies as a residue of the dislocation interactions. Nonetheless, the in-plane dislocations which have edge character, remain unaltered. This is a crucial point—we propose that when given enough thermal energy in the atomistic simulations, cross-slip of screw segments is facilitated and the dislocation density in the plastic zone substantially reduces.

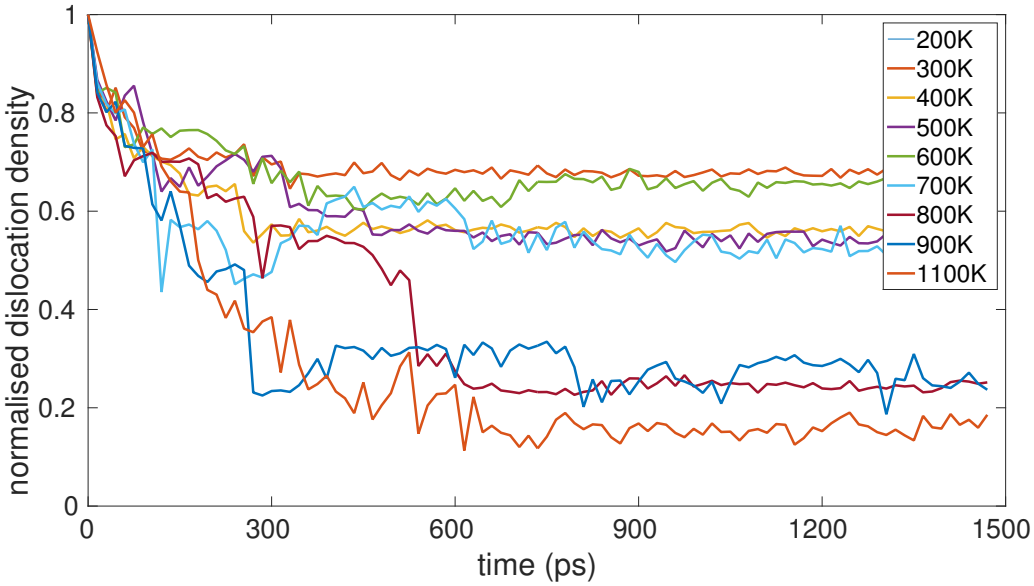

Figure 7. Normalized dislocation density during heating and waiting periods. The total dislocation length has been calculated by adding the length of perfect dislocations to half the length of partial dislocations The density is calculated by summing the total dislocation length divided by the volume of the film.

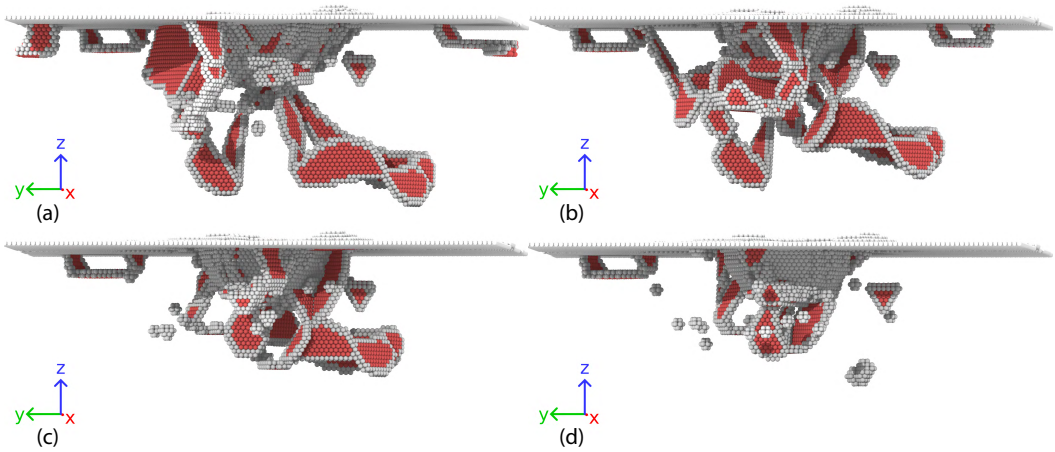

Figure 8. Dislocations microstructures at different temperatures during heating up the system up to 900 K. (**a**) at 45 K, (**b**) at 225 K, (**c**) at 585 K and (**d**) at 900 K.

The dislocation density at all temperatures does not vanish but reaches a steady-state value. Figure 9 shows the value of the steady-state dislocation density as a function of the temperature. The increasing rate by which the dislocation network is partially annihilated with temperature verifies that a thermally activated process controls the steady-state dislocation density.

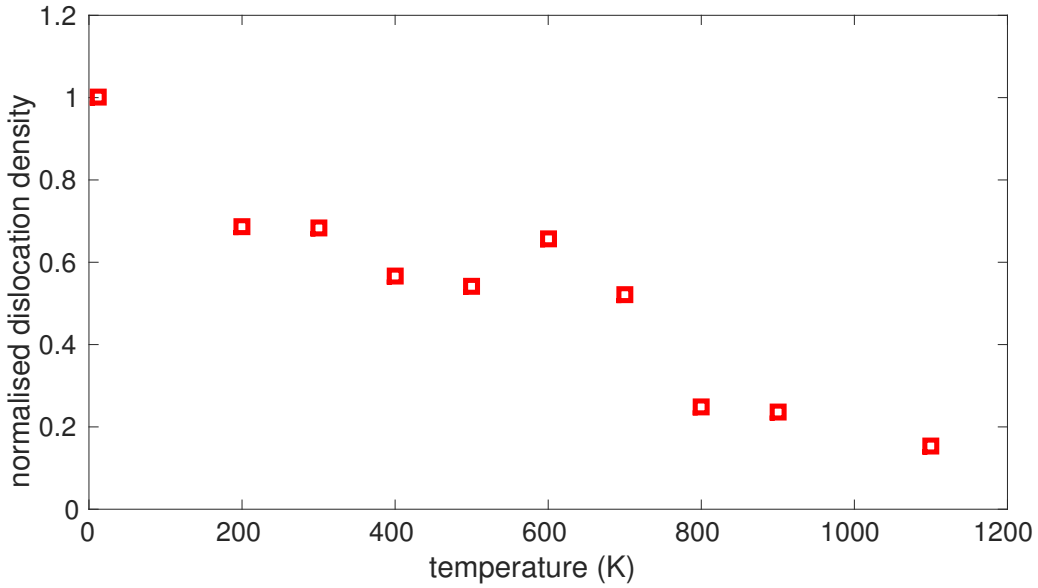

Figure 9. The normalized total dislocation length at steady states vs. temperature. The total length is calculated as the length of perfect dislocations plus half of partial dislocations.

3.3. Post-Indentation Surface Topography in the MD Simulations

If cross-slip allows some of the dislocation structure to annihilate, material should be transferred to the upper surface in order to conserve material in our simulations. Indeed, a material pile-up is identified on the upper surface of the thin films. Cross-slip allows the out-of-plane dislocations to change their slip plane and to let material glide upwards towards the free surface. The material pile-up is increased with temperature as shown in Figure 10. Here, the volume of atoms piled-up on the surface was normalized by the volume displaced by the indenter, which is equal to 87.9 nm^3 in our simulations. The volume of the pile-up is around 92% of volume displaced by the indenter at 1100 K. This is due to the fact that there are still some dislocations existing at that temperature. To summarize, the high-temperature MD simulations demonstrate how thermally activated processes

decrease the dislocation microstructure within the plastic zone, transferring the material that is displaced by the indenter to the top surface.

Figure 10b,c show the top view of material pile-up. At the end of indentation, the pile-up is localized around the indent. A large part of it is only one monoatomic layer thick, with the thickest regions being three atomic layers thick as shown in Figure 10b. On the other hand, after heating to 1100 K the pile-up is extended on the top surface and is higher above the surface as shown in Figure 10c. The pile-up at larger distances from the indent is formed due to the fact that thermally activated processes make the material flow towards the top surface far away from the plastic zone via dislocation climb. The spreading in Figure 10c clearly indicates that even a pile-up of a few monolayer can substantially contribute to the total material volume transferred to the surface, and we emphasize this since it is often ignored. However, it is worth mentioning that measuring this kind of pile-up of monolayers in experiments is challenging.

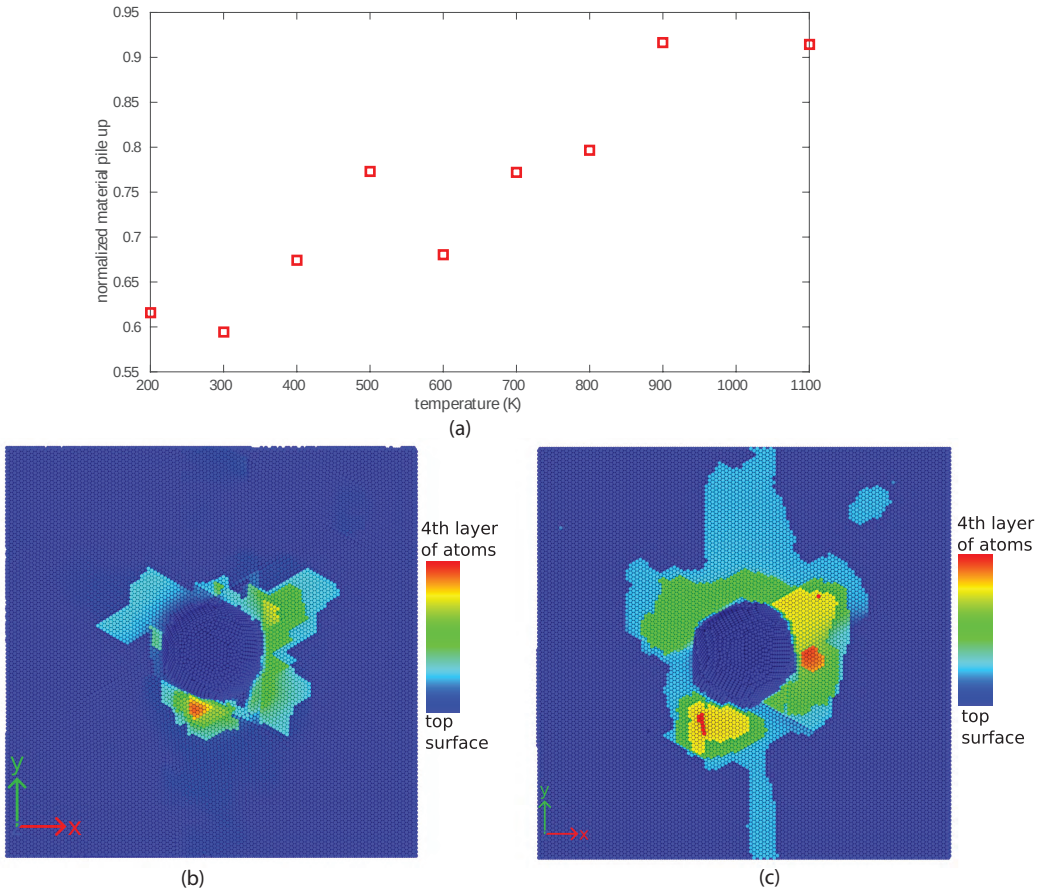

Figure 10. (**a**) Material pile-up at different temperatures under steady state conditions. (**b**,**c**) are the top view of material pile-up at the end of indentation and at 1100 K, respectively. The spreading of pile-up and its height are shown for the unheated film and at 1100 K.

4. Discussion

4.1. Experimental Results Compared to Literature

Our experiments show a reproducible deformation during very shallow indentation of gold films with the formation of an imprint and surrounding pile-up. These indents leave no or very little dislocation debris. These observations are only partially consistent with the literature.

The force-distance-curves in this work show the same features as most nanoindentation work: An elastic loading segment, followed by plastic deformation with discontinuities and a elastic unloading segment. Lilleoden and Nix [16] show that the force-distance curves

of nanoindentations of thin gold film only show discontinuities after the films have been annealed. The magnitude of these pop-ins is comparable to the ones observed here. In contrast, Ohmura et al. [34] do not observe discontinuities when performing nanoindentation in two different gold films, presumably because there are already dislocations present in these films. The force-distances curves measured by Asenjo et al. show the onset of plastic deformation at similar forces and penetration depths. The size of the discontinuities is also the same.

Asenjo et al. [7] performed similar AFM-indentation experiments in air on (111) orientated bulk Au. For indents with a depth less than 20 nm they also find no change of the surface beyond the residual imprint. For larger indents they observed the formation of terraces with atomic step height and pile-up for even larger indents. Comparing with their previous work on scanning tunneling microscopy (STM) based indentation [35], they identify the pile-up as "multiple storied" terraces. They propose a mechanism based on the nucleation and movement of screw dislocations for the imprint formation and the formation of the terraces. The discontinuities in their force-distance curves are attributed to nucleation. The proposed mechanism for the imprint is the nucleation and storage of prismatic loops in the sample.

Carrasco et al. [36] showed terraces around STM-indents on bulk (100) gold surfaces formed by screw dislocations and the motion of these dislocation during subsequent indentations. But they also observe indents with irregular pile-up, where the terraces form only during subsequent indentation in the same spot. They also show the formation of "hillocks" that form up to 100 nm from the indent and are mobile.

Filleter and Bennewitz [37] show the formation of terraces, pile-up and hillocks after indentation of bulk (100) Cu. They describe the pile-up as irregular and do not identify them as being terraces. They speculate that the nucleation of v-shaped dislocation loops causes the hillocks and the observed discontinuities in the force-distance-curve. They do not propose specific mechanisms for the pile-up formation.

In summary, the literature shows a consistent picture of the formation of terraces, pile-up and hillocks, while the latter are only observed under vacuum conditions. No long range straight glide traces are observed. All proposed models are based on dislocations that would leave debris under the indent. Since the measurements in this work are performed in air, we probably cannot distinguish between irregular and terrace-based pile-up. Despite having the resolution, we did not observe terrace formation. "Hillocks" were also not observed, but were probably below our resolution. Contrary to the literature, we see a few clear long range glide traces in the 200 nm thick film.

A possible explanation for the deviation is the stress state. The bending of the cantilever would normally lead to a lateral movement of the tip because the cantilever is inclined relative to the surface. During indentation, this movement is suppressed by the sides of the indent itself. Thus, one gets an additional force in the direction of the cantilever, leading to a different stress state and deformation mechanisms compared to perpendicular indentation with a nanoindenter. As mentioned before, the lateral force component is also a possible explanation for the region IV in the force-distance, since a significant reduction of this region was observed when the lateral movement was actively compensated.

4.2. Annihilation of the Dislocation Structure in the Plastic Zone

Cross-slip allows constricted screw segments to change their slip plane and annihilate some of the dislocation structures. However, while nucleation and glide are naturally described in the MD simulations, the system was heated to temperatures much higher than the experimental conditions, in order to accelerate cross-slip within the time frames of the MD simulations (nanoseconds). For this reason, we heated the system while keeping the tip inside the specimen. Heating leads to thermal expansion, and although the goal was to keep the load constant while heating, it cannot be maintained perfectly constant. For this reason, we allowed the lateral stress along the periodic boundary conditions to relax during heating. This process indeed changes the load, but the thermal expansion results

in load decrease, which is closer to what is happening in the experiments when pulling out the indent. As a result, it is difficult to differentiate between the contribution of load removal to the decrease in the dislocation density and cross-slip events. Nonetheless, since the TEM observations are obtained after load removal, the MD simulations highlight that both phenomena may lead to annihilation of the dislocation structure, even if we are not able to quantify the contribution of each mechanism.

With that being said, we can estimate the cross-slip rate under experimental conditions, to see if it is within an order of magnitude of what is needed to account for the dislocation densities observed in the experiments. In order to examine the rate of cross-slip at room temperature, let us estimate the energy barrier for cross-slip beneath the indent. While we are not familiar with information on the energy barriers for cross-slip in Au, we can estimate the activation parameters based on those of Cu, using line tension models [38]. The activation energy for cross-slip of a jogged screw dislocation in Cu was found in atomistic simulations to be equal to $E_{Cu} = 1.2$ eV. In addition, it was shown in [39] that the activation energy barrier for cross-slip of an unstressed screw dislocation is proportional to $\frac{(\mu b^2)^2}{\gamma}$, where μ is the shear modulus, b is the magnitude of the Burgers vector and γ is the stacking fault energy. Consequently, the activation barrier for cross-slip in Au can be calculated from the value in Cu,

$$E_{Au} = E_{Cu}\frac{(\mu_{Au}b_{Au}^2)^2\gamma_{Cu}}{(\mu_{Cu}b_{Cu}^2)^2\gamma_{Au}} \quad (1)$$

When considering the following values: $\mu_{Au} = 31\,\text{GPa}$, $b_{Au} = 0.288\,\text{nm}$, $\gamma_{Au} = 32\ \text{mJ m}^{-2}$, $\mu_{Cu} = 54.6\,\text{GPa}$, $b_{Cu} = 0.255\,\text{nm}$ and $\gamma_{Cu} = 45\,\text{mJ m}^{-2}$, the activation energy barrier for cross-slip in Au is found to be $E_{Au} = 0.88\,\text{eV}$. However, the dislocation structure generated beneath the indent results from the indenter stress field as well as from dislocation interactions. The free energy barrier of a stressed screw dislocation is lower than the value found in Equation (1) and is equal to $E_{Au} - \sigma V_{Au}$, where V_{Au} is the activation volume for cross-slip in Au. For Cu, it was found that the activation volume is $V_{Cu} = 15b_{Cu}^3$ [40]. The activation volume was proposed to be proportional to $d_0^2 b$, where d_0 is the dissociation width of an unstressed screw dislocation [41]. According to isotropic elasticity theory d_0 is proportional to $\mu b^2(2-3\nu)/\gamma(1-\nu)$. Thereupon, the activation volume for cross-slip in Au satisfies,

$$V_{Au} = V_{Cu}\frac{\mu_{Au}^2 b_{Au}^5 \gamma_{Cu}^2}{\mu_{Cu}^2 b_{Cu}^5 \gamma_{Au}^2}\left(\frac{(2-3\nu_{Au})(1-\nu_{Cu})}{(2-3\nu_{Cu})(1-\nu_{Au})}\right)^2 \quad (2)$$

Considering $\nu_{Cu} = 0.324$ and $\nu_{Au} = 0.412$, the activation volume for cross-slip in Au is estimated to be $V_{Au} = 8.9b_{Au}^3$. We note that the value of V_{Cu} was found for non-jogged dislocations and is extracted for the stresses between screw dislocations in a dipole structure. However, this value is within the range of other expectations, and is an order of magnitude smaller than the values found experimentally [42,43]. Finally, we adopt transition state theory to estimate the cross-slip rate under the indent. The annihilation rate is assumed to follow Arrhenius law

$$f = f_0\, e^{-\frac{E_{Au}-\sigma V_{Au}}{kT}} \quad (3)$$

where f_0 is the rate prefactor and kT has its usual meaning. We consider the same rate prefactor per dislocation unit length found for Cu , $f_0 = 4 \times 10^{13}\ \text{Hz b}^{-1}$. Keeping in mind the activation parameters estimated above, the cross-slip rate at room temperature for various stresses can be found. For instance, for a screw segment of length of 100 b_{Au}, the rate of cross-slip events somewhere along the line is of the order of 1 Hz under no stress. However, if the stress applied on the screw segment from the indent and the surrounding microstructure is of the order of 100 MPa, the cross-slip rates increase and are of the order of 10^3 Hz. For a stress of 200 MPa, the rates increase even more to the order of 10^5 Hz etc. These stress levels are expected to be found beneath the indenter for Au [44]. Thus, at these

high rates, it is very likely to see substantial number of cross-slip events within the time of the experiment at room temperature.

It is worth pointing out that cross-slip does not affect the half prismatic loops which glide parallel to the upper facet, since these are purely of edge character. In a previous study, we showed that these loops can be annihilated via climb to the upper surface [45]. Therefore, climb can also assist in the annihilation of the dislocation microstructure. However, climb is a slow process and will probably affect mainly the small loops in the experimental conditions. In summary, we proposed that load removal and cross-slip eliminate most of the dislocation structure around the indent, but some half prismatic loops glide parallel to the surface away from the indent, and they remain even after load removal, as observed in the TEM images (Figure 4b).

4.3. Material Transfer to the Upper Surface

As a result of the substantial cross-slip and the reverse plasticity of dislocation glide back towards the surface during load removal, material "flows" upwards to the upper surface. The importance of cross-slip to material pile-up around the indent was recognized previously in nanoindentation of Au nanoparticles and thin films [25]. When lateral free surfaces are present in the specimen, as in nanoparticles, dislocations nucleate and glide relatively easily towards the lateral surfaces instead of accumulating beneath the indent. Consequently, the material did not pile-up on the upper surface but expanded laterally. On the other hand, a clear material pile-up was identified during nanoindentation of thin films of the same height as the nanoparticles. The material pile-up is attributed to the fact that dislocations accumulate beneath the indent and have sufficient time to cross-slip.

The material pile-up owing to cross-slip was also observed in the MD simulations presented here. The material was not localized close to the indent but was spread out over a wide region. For instance, at the maximum indentation depth of 3.36 nm and for the highest temperature simulated, the maximum height of the pile-up was only a few atomic layers (Figure 10b). However, at intermediate loads, a significant material pile-up was not identified in the experiments. In order to estimate the height of the material pile-up at these loads, let us assume that all dislocations were annihilated via thermally activated processes, i.e. the volume of the imprint is equal to the volume of the pile-up. Assuming a spherical indent, the volume pushed by the indenter is $\pi\delta^2(R-\delta/3)$, where δ is the indentation depth and R is the tip radius as shown in Figure 11. For simplicity, it is assumed that the material added on the upper surface is spread in a cylindrical volume of height h and radius l. The volume of the material in the pile-up is equal to $\pi h(l^2-a^2)$ where a, the radius of the imprint, satisfies $a^2=\delta(2R-\delta)$. The comparison between these volumes leads to a pile-up height that satisfies

$$\frac{h}{\delta}=\frac{1}{3}\frac{\delta(3R-\delta)}{l^2-\delta(2R-\delta)} \tag{4}$$

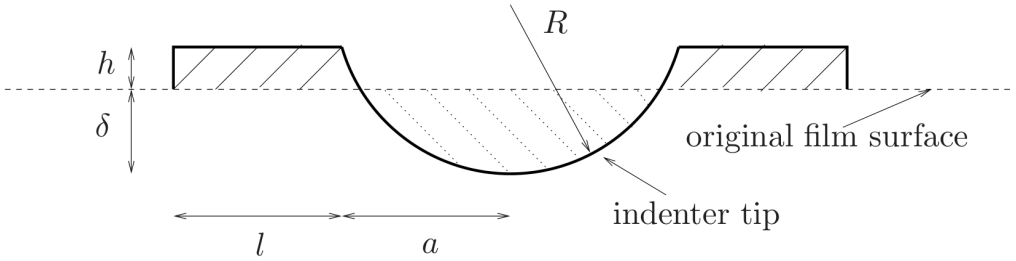

Figure 11. Schematic illustration of the material pile-up around the indent. The volume pushed by the indenter is marked with slanted dashed lines, and the material pile-up with slanted solid lines.

The value of l depends on the various dislocation mechanisms beneath the indent. Nonetheless, for the current discussion, a value of $l=2a$ will be considered, based on the

MD results shown in Figure 10b,c. As an example, for the experiment with the maximum load of 3 μN, which corresponds to an indentation depth of $\delta = 12$ nm, the height of the pile-up according to Equation (4) is 0.7 nm, which is only about 3 monolayers. Consequently, we conclude that even if thermally activated processes annihilate all dislocations within the bulk and the material is flowing upwards and spreads around the indent, at intermediate loads we expect the material pile-up to be only of a few monolayers in height on average. In practice, not all dislocations are annihilated, so that these average heights are even smaller than the estimations given here. Additionally, material pile-up is not spread homogeneously, as was reported in deep indentation experiments (e.g., [33,46,47]) and also in the MD simulations shown in Figure 10. The predictions of this simple volume conserving model are consistent with the pile-up heights obtained from both experiments and simulations, strengthening the idea that pile-up occurs by the dislocation cross-slip mediated transfer of material from under the indent to the surface.

5. Conclusions

To summarize, we have shown that very shallow indentation in gold thin films leads to well-defined stages of elastic and plastic response and leaves surface imprints that are consistent with the measured plastic strain. However, post-mortem investigations with AFM and TEM show an absence of the expected stored dislocations needed to account for the plastic strain. Molecular dynamics was able to resolve this conflict by revealing that cross-slip leads to the annihilation of dislocations and the transfer of material to the surface around the indent. Long range glide and dislocation pile-ups play relatively unimportant roles. The dominance of dislocation-dislocation interactions under the indent overshadows interactions with interfaces and boundaries, accounting for the fact that no effect of film thickness was observed.

The lack of dislocation storage under the shallow indents observed here has important implications for the wear of metal surfaces. Macroscopic contact between two surfaces involves actual contact at asperities, many of which are as small as the nanoscale contacts investigated here with AFM. Our studies reveal that these contacts result in plasticity but do not generate stored dislocations, thereby bypassing the positive effects of work hardening. Based on the mechanistic insights gained from the molecular dynamics studies, we propose the rather intuitive idea that closely spaced pinning sites in the near surface region might be able to hinder the annihilation of dislocations, increasing work hardening and reducing wear of metal surfaces.

Author Contributions: investigation, S.R., S.W.; writing—original draft preparation, S.R., S.W.; writing—review and editing, D.M., C.A.V.; supervision, D.M., C.A.V. All authors have read and agreed to the published version of the manuscript.

Funding: We are grateful for funding from the German Science Foundation (Deutsche Forschungsgemeinschaft—DFG) through the collaborative research center CRC 602 "Komplexe Strukturen in kondensierter Materie von atomarer bis mesoskopischer Skala".

Institutional Review Board Statement: Not applicable.

Informed Consent Statement: Not applicable.

Data Availability Statement: The data that support the findings of this study are available from the corresponding author on request.

Acknowledgments: We thank Felix Schlenkrich for the preparation of the Au thin films on SiN_x.

Conflicts of Interest: The authors declare no conflict of interest.

References

1. Zemła, J.; Bobrowska, J.; Kubiak, A.; Zieliński, T.; Pabijan, J.; Pogoda, K.; Bobrowski, P.; Lekka, M. Indenting soft samples (hydrogels and cells) with cantilevers possessing various shapes of probing tip. *Eur. Biophys. J.* **2020**, *49*, 485–495. [CrossRef]
2. Qian, L.; Zhao, H. Nanoindentation of Soft Biological Materials. *Micromachines* **2018**, *9*, 654. [CrossRef] [PubMed]

3. Doss, B.L.; Rahmani Eliato, K.; Lin, K.h.; Ros, R. Quantitative mechanical analysis of indentations on layered, soft elastic materials. *Soft Matter* **2019**, *15*, 1776–1784. [CrossRef] [PubMed]
4. Cortelli, G.; Patruno, L.; Cramer, T.; Murgia, M.; Fraboni, B.; de Miranda, S. Atomic Force Microscopy Nanomechanics of Hard Nanometer-Thick Films on Soft Substrates: Insights into Stretchable Conductors. *ACS Appl. Nano Mater.* **2021**, *4*, 8376–8382. [CrossRef] [PubMed]
5. Liu, Y.; Sokolov, I.; Dokukin, M.E.; Xiong, Y.; Peng, P. Can AFM be used to measure absolute values of Young's modulus of nanocomposite materials down to the nanoscale? *Nanoscale* **2020**, *12*, 12432–12443. [CrossRef]
6. Falin, A.; Cai, Q.; Santos, E.J.G.; Scullion, D.; Qian, D.; Zhang, R.; Yang, Z.; Huang, S.; Watanabe, K.; Taniguchi, T.; et al. Mechanical properties of atomically thin boron nitride and the role of interlayer interactions. *Nat. Commun.* **2017**, *8*, 15815. [CrossRef]
7. Asenjo, A.; Jaafar, M.; Carrasco, E.; Rojo, J.M. Dislocation mechanisms in the first stage of plasticity of nanoindented Au(111) surfaces. *Phys. Rev. B* **2006**, *73*, 075431. [CrossRef]
8. Navarro, V.; Rodríguez de la Fuente, O.; Mascaraque, A.; Rojo, J.M. Uncommon Dislocation Processes at the Incipient Plasticity of Stepped Gold Surfaces. *Phys. Rev. Lett.* **2008**, *100*, 105504. [CrossRef]
9. Tranchida, D.; Piccarolo, S. Combining Atomic Force Microscopy and Depth-Sensing Instruments for the Nanometer-Scale Mechanical Characterization of Soft Matter. In *Scanning Probe Microscopy in Nanoscience and Nanotechnology*; Bhushan, B., Ed.; Springer: Berlin/Heidelberg, Germany, 2010; pp. 199–223. [CrossRef]
10. Filleter, T.; Maier, S.; Bennewitz, R. Atomic-scale yield and dislocation nucleation in KBr. *Phys. Rev. B* **2006**, *73*, 155433. [CrossRef]
11. Egberts, P.; Bennewitz, R. Atomic-scale nanoindentation: Detection and identification of single glide events in three dimensions by force microscopy. *Nanotechnology* **2011**, *22*, 425703. [CrossRef]
12. Caron, A. Quantitative Hardness Measurement by Instrumented AFM-indentation. *JoVE* **2016**, *117*, e54706. [CrossRef] [PubMed]
13. Amat, E.; del Moral, A.; Fernández-Regúlez, M.; Evangelio, L.; Lorenzoni, M.; Gharbi, A.; Rademaker, G.; Pourteau, M.L.; Tiron, R.; Bausells, J.; et al. Exploring Strategies to Contact 3D Nano-Pillars. *Nanomaterials* **2020**, *10*, 716. [CrossRef] [PubMed]
14. Ohmura, T.; Wakeda, M. Pop-In Phenomenon as a Fundamental Plasticity Probed by Nanoindentation Technique. *Materials* **2021**, *14*, 1879. [CrossRef] [PubMed]
15. Dietiker, M.; Nyilas, R.D.; Solenthaler, C.; Spolenak, R. Nanoindentation of single-crystalline gold thin films: Correlating hardness and the onset of plasticity. *Acta Mater.* **2008**, *56*, 3887–3899. [CrossRef]
16. Lilleodden, E.T.; Nix, W.D. Microstructural length-scale effects in the nanoindentation behavior of thin gold films. *Acta Mater.* **2006**, *54*, 1583–1593. [CrossRef]
17. Graça, S.; Carvalho, P.A.; Colaço, R. Dislocation structures in nanoindented ductile metals—A transmission electron microscopy direct observation. *J. Phys. D Appl. Phys.* **2011**, *44*, 335402. [CrossRef]
18. Gouldstone, A.; Koh, H.J.; Zeng, K.Y.; Giannakopoulos, A.E.; Suresh, S. Discrete and continuous deformation during nanoindentation of thin films. *Acta Mater.* **2000**, *48*, 2277–2295. [CrossRef]
19. Nix, W.D.; Gao, H. Indentation size effects in crystalline materials: A law for strain gradient plasticity. *J. Mech. Phys. Solids* **1998**, *46*, 411–425. [CrossRef]
20. Kelchner, C.L.; Plimpton, S.J.; Hamilton, J.C. Dislocation nucleation and defect structure during surface indentation. *Phys. Rev. B* **1998**, *58v*, 11085–11088. [CrossRef]
21. Chang, H.J.; Fivel, M.; Rodney, D.; Verdier, M. Multiscale modelling of indentation in FCC metals: From atomic to continuum. *C. R. Phys.* **2010**, *11*, 285–292. [CrossRef]
22. Kositski, R.; Mordehai, D. Depinning-controlled plastic deformation during nanoindentation of BCC iron thin films and nanoparticles. *Acta Mater.* **2015**, *90*, 370–379. [CrossRef]
23. Fivel, M.; Robertson, C.; Canova, G.; Boulanger, L. Three-dimensional modeling of indent-induced plastic zone at a mesoscale. *Acta Mater.* **1998**, *46*, 6183–6194. [CrossRef]
24. Gagel, J.; Weygand, D.; Gumbsch, P. Formation of extended prismatic dislocation structures under indentation. *Acta Mater.* **2016**, *111*, 399–406. [CrossRef]
25. Roy, S.; Gatti, R.; Devincre, B.; Mordehai, D. A multiscale study of the size-effect in nanoindentation of Au nanoparticles. *Comput. Mater. Sci.* **2019**, *162*, 47–59. [CrossRef]
26. Durst, K.; Backes, B.; Göken, M. Indentation size effect in metallic materials: Correcting for the size of the plastic zone. *Scr. Mater.* **2005**, *52*, 1093–1097. [CrossRef]
27. Zhang, J.-I.; Zaefferer, S.; Raabe, D. A study on the geometry of dislocation patterns in the surrounding of nanoindents in a TWIP steel using electron channeling contrast imaging and discrete dislocation dynamics simulations. *Mater. Sci. Eng. A* **2015**, *636*, 231–242. [CrossRef]
28. Walters, D.A.; Cleveland, J.P.; Thomson, N.H.; Hansma, P.K.; Wendman, M.A.; Gurley, G.; Elings, V. Short cantilevers for atomic force microscopy. *Rev. Sci. Instruments* **1996**, *67*, 3583–3590. [CrossRef]
29. Grochola, G.; Russo, S.P.; Snook, I.K. On fitting a gold embedded atom method potential using the force matching method. *J. Chem. Phys.* **2005**, *123*, 204719. [CrossRef]
30. Xia, W.; Dehm, G.; Brinckmann, S. Unraveling indentation-induced slip steps in austenitic stainless steel. *Mater. Des.* **2019**, *183*, 108169. [CrossRef]

31. Roa, J.; Oncins, G.; Dias, F.; Vieira, V.; Schaf, J.; Segarra, M. AFM as an alternative for Young's modulus determination in ceramic materials in elastic deformation regime. *Phys. C Supercond.* **2011**, *471*, 544–548. [CrossRef]
32. Gao, N.; Perez, D.; Lu, G.; Wang, Z. Molecular dynamics study of the interaction between nanoscale interstitial dislocation loops and grain boundaries in BCC iron. *J. Nucl. Mater.* **2018**, *498*, 378–386. [CrossRef]
33. Mordehai, D.; Kazakevich, M.; Srolovitz, D.J.; Rabkin, E. Nanoindentation size effect in single-crystal nanoparticles and thin films: A comparative experimental and simulation study. *Acta Mater.* **2011**, *59*, 2309–2321. [CrossRef]
34. Ohmura, T.; Matsuoka, S.; Tanaka, K.; Yoshida, T. Nanoindentation load-displacement behavior of pure face centered cubic metal thin films on a hard substrate. *Thin Solid Film* **2001**, *385*, 198–204. [CrossRef]
35. Carrasco, E.; Rodríguez de la Fuente, O.; González, M.A.; Rojo, J.M. Dislocation cross slip and formation of terraces around nanoindentations in Au(001). *Phys. Rev. B* **2003**, *68*, 180102. [CrossRef]
36. Carrasco, E.; González, M.; Rodríguez de la Fuente, O.; Rojo, J. Analysis at atomic level of dislocation emission and motion around nanoindentations in gold. *Surf. Sci.* **2004**, *572*, 467–475. [CrossRef]
37. Filleter, T.; Paul, W.; Bennewitz, R. Atomic structure and friction of ultrathin films of KBr on Cu(100). *Phys. Rev. B* **2008**, *77*, 035430. [CrossRef]
38. Malka-Markovitz, A.; Mordehai, D. Cross-slip in face-centered cubic metals: A general Escaig stress-dependent activation energy line tension model. *Philos. Mag.* **2018**, *98*, 347–370. [CrossRef]
39. Landau, P.; Mordehai, D.; Venkert, A.; Makov, G. Universal strain–temperature dependence of dislocation structures at the nanoscale. *Scr. Mater.* **2012**, *66*, 135–138. [CrossRef]
40. Vegge, T.; Jacobsen, K.W. Atomistic simulations of dislocation processes in copper. *J. Phys. Condens. Matter* **2002**, *14*, 2929–2956. [CrossRef]
41. Caillard, D.; Martin, J. (Eds.) *Thermally Activated Mechanisms in Crystal Plasticity*; Pergamon: Oxford, UK, 2003.
42. Bonneville, J.; Escaig, B.; Martin, J. A study of cross-slip activation parameters in pure copper. *Acta Metall.* **1988**, *36*, 1989–2002. [CrossRef]
43. Bonneville, J.; Escaig, B. Cross-slipping process and the stress-orientation dependence in pure copper. *Acta Metall.* **1979**, *27*, 1477–1486. [CrossRef]
44. Tangena, A.G.; Hurkx, G.A.M. The Determination of Stress-Strain Curves of Thin Layers Using Indentation Tests. *J. Eng. Mater. Technol.* **1986**, *108*, 230–232. [CrossRef]
45. Roy, S.; Mordehai, D. Annihilation of edge dislocation loops via climb during nanoindentation. *Acta Mater.* **2017**, *127*, 351–358. [CrossRef]
46. Pathak, S.; Riesterer, J.L.; Kalidindi, S.R.; Michler, J. Understanding pop-ins in spherical nanoindentation. *Appl. Phys. Lett.* **2014**, *105*, 161913. [CrossRef]
47. Kucharski, S.; Jarząbek, D. Depth Dependence of Nanoindentation Pile-Up Patterns in Copper Single Crystals. *Metall. Mater. Trans. A* **2014**, *45*, 4997–5008. [CrossRef]